

Geologica Acta: an international earth science journal

ISSN: 1695-6133 ISSN: 1696-5728

geologica-acta@ictja.csic.es

Universitat de Barcelona

España

Peral, M.; Fernàndez, M.; Torne, M.
Resolution test of GOCE satellite data applied to density anomalies at crustal and upper mantle levels
Geologica Acta: an international earth science journal,
vol. 16, no. 1, 2018, January-March, pp. 93-105
Universitat de Barcelona
España

DOI: https://doi.org/10.1344/GeologicaActa2018.16.1.6

Available in: https://www.redalyc.org/articulo.oa?id=50558534006



Complete issue

More information about this article

Journal's webpage in redalyc.org



Scientific Information System Redalyc

Network of Scientific Journals from Latin America and the Caribbean, Spain and Portugal

Project academic non-profit, developed under the open access initiative

Resolution test of GOCE satellite data applied to density anomalies at crustal and upper mantle levels

M. PERAL¹ M. FERNÀNDEZ¹ M. TORNE¹

¹Group of Dynamics of the Lithosphere, Institute of Earth Sciences Jaume Almera, ICTJA-CSIC C/ Lluís Solé i Sabarís s/n, 08028 Barcelona, Spain. Peral E-mail: mperal@ictja.csic.es

The Gravity field and steady-state Ocean Circulation Explorer (GOCE) satellite mission was devised by the European Space Agency to study the Earth's gravity field with an unprecedented accuracy using gravity gradient data. The goal of this study is to analyze the resolution in terms of size, burial depth and density contrast of anomalous bodies related to geological structures that can be identified from GOCE data. A parametric study is performed by calculating the gravity gradients associated with rectangular prisms with fixed aspect ratio of 9:3:1 and varying the size, burial depth, and density contrast, selecting those structures showing amplitudes and wavelength variations comparable to the accuracy of GOCE data. Results show that the minimum size for crustal anomalies to be resolved for the vertical component of the gravity gradient is 22.5x7.5x2.5km for a $\Delta \rho = 500kg/m^3$, burial depth of 0km, and at computation height of 255km. To generate a sufficient signal in amplitude and wavelength in all the components, the size of the anomalous body is 270x90x30km. For a body with $\Delta \rho = 50kg/m^3$ and 0km burial depth a minimum size of 41.4x13.8x4.6km is required for the vertical component at a computation height of 255km. In addition, the application to the 3D case of a passive continental margin which broadly resembles the crustal structure of the NW-Iberia shows that the signal of all gravity gradient components is dominated by the crustal thinning associated with the passive continental margins and the corresponding isostatic response.

KEYWORDS

GOCE. Gravity gradients. Geological structures resolution. NW Iberian margin.

INTRODUCTION

The Gravity field and steady-state Ocean Circulation Explorer (GOCE) (Floberghagen *et al.*, 2011) is one of the last satellite missions launched by the European Space Agency (ESA) to provide new insights on a broad range of issues, from oceanography to solid Earth physics as well as sea-level and climate change.

The main novelty of GOCE with respect to previous missions is the measurement of gravity gradients, *i.e.* the second derivate of the gravitational potential (V),

$$G_{ii} = -(\delta^2 V)/(d_i d_i)$$
 (1)

where i,j = x,y,z, representing the spatial rate of change of the gravity vector, \vec{g} , in all three perpendicular directions (Saad, 2006). The Electrostatic Gravity Gradiometer (EGG) from GOCE (van der Meijde *et al.*, 2015a) is the most important and innovative instrument of the satellite, allowing for direct measurements of the spatial variations of the Earth's gravity field with a great high accuracy (about 10^{-13} of the gravitational attraction on Earth). Original and final GOCE products as well as details of the different coordinate systems used to represent gravity gradients can be found in the literature (*e.g.* Fuchs and Bouman, 2011; Bouman and Fuchs, 2012; Bouman *et al.*, 2013; Fecher *et al.*, 2015; Bouman *et al.*, 2016).

The GOCE mission was launched on March 2009 and ended on October 2013, generating great expectations since the very beginning. The first gravity model derived from GOCE was presented in June 2010. The potential of the mission to improve the estimated mean circulation of the North Atlantic was envisaged very soon, two months after initiating the satellite measurements (Bingham *et al.*, 2011). One of the products of GOCE is the global GOCO03S model, a great-accuracy and high-resolution global gravity field model that combines GOCE, GRACE, SLR and CHAMP satellite data. GOCO03S model is a spherical harmonics expansion model developed up to degree 250 with a half-wavelength spatial resolution of 80km and accuracy of 0.4mE in gravity gradients at orbit altitude (255km) (Mayer-Gürr *et al.*, 2012).

Several studies revealed that the gravity gradients signal may become relevant in modelling the lithosphere and upper mantle density variations (Hirt et al., 2012; Mariani et al., 2013; Fullea et al., 2014, 2015; Bouman et al., 2015; Fadel et al., 2015; Reguzzoni and Sampietro, 2015; Barzaghi et al., 2016). GOCE data have been also used to explore the crustal and upper mantle structures in Africa (Martinec and Fullea, 2015), Arabia (Holzrichter and Ebbing, 2016) and the Andean and Central American margins (Köther et al., 2012) among many other regions. Finally, a number of studies are devoted to validate the quality and accuracy of the GOCE data (e.g. Godah and Krynski, 2013; Braitenberg et al., 2013; Fecher et al., 2015; Mysen, 2015; Pal and Majumdar, 2015). A summary describing the studies based on the GOCE mission can be found in van der Meijde et al. (2015b). Nevertheless, to our knowledge, a parametric study focusing on the size, burial depth, and density contrast of anomalous bodies that can be resolved from GOCE gravity gradients data at crust and upper mantle levels is still missing, being this the main goal of our work.

We have first computed the gravity gradients that are related to rectangular prism structures of different size, burial depth, and density contrast. Second, we have computed the gravity gradients corresponding to a synthetic 3D passive continental margin structure. We have compared the resulting signal with that calculated from the GOCO03S gravity potential model in the NW Iberian margin, which has a similar crustal structure. Results are discussed in terms of possible geological structures that can be resolved from GOCE data and the gravity gradient signature associated with these structures.

RESOLUTION OF SINGLE-PRISM DENSITY ANOMALIES

To compute the gravity gradients from synthetic models we have used the *Tesseroids* approach developed

by Uieda *et al.* (2015). *Tesseroids* is a forward modelling software of gravitational fields that supports models and computation grids in Cartesian (planar approximation) or spherical coordinates, in which the geometric element can be either a sphere (tesseroid) or a rectangular prism. In our estimations, we have considered both the planar and the spherical approximation. Although the spherical approximation gives a more exact solution, our results fully agree with those obtained by Fullea *et al.* (2015) in that the difference between both approximations is close to the GOCE resolution (1mE, 1milli-Eötvös = 10^{-12} s⁻²) when calculations are made at the satellite altitude (255km) and the lateral dimensions of the anomalous body are in the range of 1°x1°. To what follows we will show the results from the spherical approximation.

The performed tests consist to identify those density anomalies with the minimum size and density contrast that, at the mean satellite altitude (255km), show a gravity gradient with an amplitude larger than GOCE resolution (1mE for the accurate components G_{xx} , G_{yy} , G_{zz} , G_{xz} and 100mE for G_{xy} and G_{yz}), and a sufficient wavelength to recognize the shape of the anomaly. Therefore, we have defined a series of rectangular prisms (Fig. 1) with a fixed aspect ratio of 9:3:1, length (Δx), width (Δy), and thickness (Δz), respectively. The variables of the model are the dimensions of the prism (Δx , Δy , Δz), the burial depth (z_1) and the density contrast ($\Delta \rho$).

To maximize the gravity effects, we have considered two end-member density contrast values for crust and upper mantle levels. Density contrasts of up to $\Delta \rho = 500 \text{kg/m}^3$ are restricted to crustal levels and can be either associated with uncompacted sedimentary basins (e.g. young marine

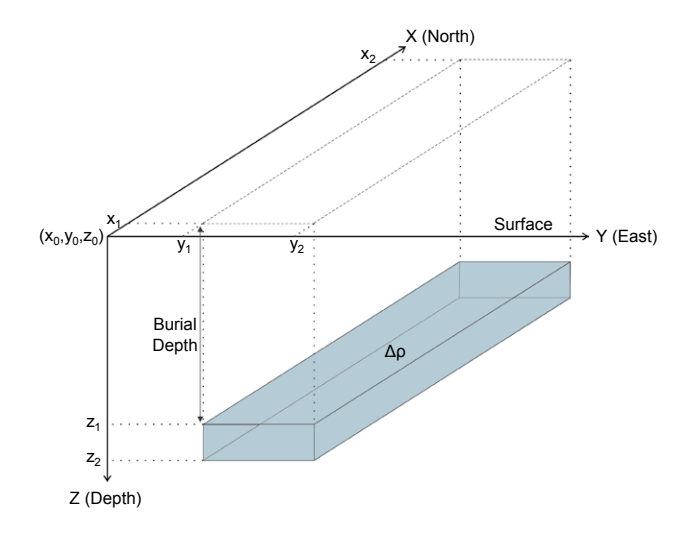


FIGURE 1. Scheme representing a rectangular prism with aspect ratio 9:3:1, corresponding to the anomalous bodies modelled in this study. The coordinate system has the X axis pointing North, the Y axis to the East and the Z axis the depth. $\Delta \rho$: density contrast.

basins, salt diapirs), or with variations of the crust-mantle boundary topography (*i.e.* Moho depth) (*e.g.* Christensen and Mooney, 1995; Brocher, 2005; Torne *et al.*, 2015). Larger density contrasts about 1600–1700kg/m³ (*e.g.* lakes and ocean basins) or 2400–2670kg/m³ (*e.g.* topography effect) are always found at superficial levels and can cause perturbations in the gravity gradient, about ±3E (*e.g.* Holzrichter and Ebbing, 2016).

A density contrast of $\Delta p=50 \text{kg/m}^3$ can be expected at any depth within the crust, related to lithological variations (*e.g.* Barton, 1986; Christensen and Mooney, 1995; Maystrenko and Scheck-Wenderoth, 2009), or within the upper mantle related to thermal and/or compositional variations (Cammarano *et al.*, 2011; Afonso *et al.*, 2013; Globig *et al.*, 2016).

Amplitude resolution

In the first test the anomalous body has a density contrast of 500kg/m^3 and a burial depth z_1 covering the common range of crustal depth, *i.e.* $0 \le z_1 \le 40 \text{km}$. After estimations, we find that the minimum dimensions of the anomalous body that can be resolved by the G_{zz} component within this depth range is $\Delta x = 22.5 \text{km}$, $\Delta y = 7.5 \text{km}$, and $\Delta z = 2.5 \text{km}$. The resulting maximum value of the G_{zz} component is 1.7mE, if the anomalous body is located at the Earth's surface $(z_1 = 0 \text{km})$ and 1.1mE when the burial depth is $z_1 = 40 \text{km}$ (Fig. 2). Note that, at this depth, the gradient signal is in the limit of GOCE resolution (1mE).

In the second test, the anomalous body has a density contrast of 50kg/m³ and a burial depth z₁ covering the whole range of crust and upper mantle depths, i.e. $0 \le z_1 \le 650$ km. In this case, the minimum size that results in a perceptible signature in the vertical component of the gravity gradient ($G_{xz}=1$ mE) is 41.4x13.8x4.6km and occurs for z_1 =0. As the considered density contrast can occur at any depth within the crust and the upper mantle, were interested in determining the minimum size of the anomalous body that can be detected at different depths (see Table 1). Figure 3A plots depth vs. thickness of the anomalous body that produces a vertical gravity gradient signal of $G_{yz}=1$ mE. We find that there is a linear relationship between both variables when using the fixed aspect ratio of 9:3:1. Therefore, an anomalous body within the lithospheric mantle (i.e. $50 \text{km} \le z_1 \le 200 \text{km}$) requires minimum dimensions of $\Delta x=49.5-75.6$ km; $\Delta y=16.5-25.2$ km; and $\Delta z=5.5-8.4$ km, respectively. For anomalies located in the upper mantle, at 400km and 650km depth, the minimum thickness values required are 12.3 and 17.5km, respectively. At the crustal depth range (0-40km), the wavelength of the G_{zz} anomalies with similar amplitudes do not differ noticeably, but they do when the burial depth is in the range of hundred

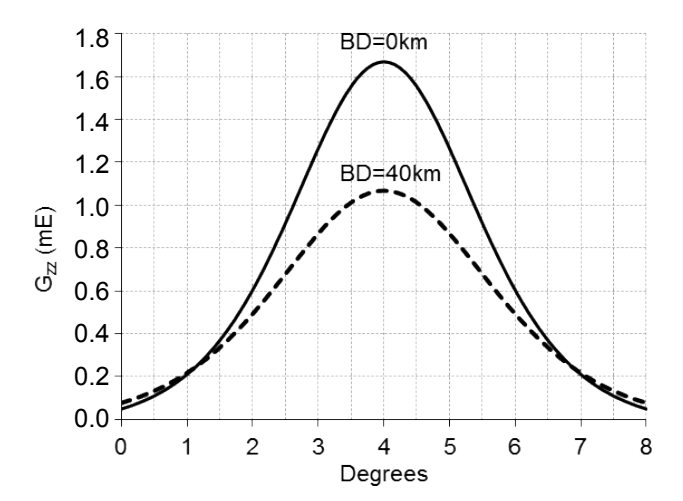


FIGURE 2. Gravity gradients G_{zz} (vertical axis) generated by an anomalous density body. The horizontal axis represents the East direction. The size of the body is Δx =22.5km, Δy =7.5km, Δz =2.5km, with a density contrast of 500kg/m³ and Burial Depths (BD) of 0 and 40km. The density anomaly is calculated at the mean satellite altitude of 255km.

kilometers (Fig. 3B). The resulting half wavelength (>400km) exceeds by far the spatial resolution of GOCE (80km).

Wavelength resolution

In the previous section, we have shown the minimum size and burial depth of a density anomaly producing a detectable gravity gradient signal in the G_{zz} component. However, both size and burial depth of the density anomaly influence in a different way the wavelength of the gravity gradient variations and particularly, the spatial distribution of maximum and minimum (extrema) values. Figure 4 shows the six gravity gradient components for an anomalous density body of 22.5x7.5x2.5km, $\Delta \rho = 500kg/m^3$ and burial depth $z_1 = 0km$ computed at 5km height. The G_{zz} component delineates a maximum value miming the planar shape of the density anomaly, whereas the

TABLE 1. Resulting dimensions of an anomalous density body with a density contrast of 50kg/m³ at different burial depths

BDa(km)	$\Delta x^b(km)$	$\Delta y^b (km)$	$\Delta z^{\rm c}(km)$	$G_{zzmax}{}^{d}(mE)$
0	41.4	13.8	4.6	1.0
0	49.5	16.5	5.5	1.7
40	49.5	16.5	5.5	1.1
100	58.5	19.5	6.5	1.0
200	75.6	25.2	8.4	1.0
300	92.7	30.9	10.3	1.0
400	110.7	36.9	12.3	1.0
650	157.5	52.5	17.5	1.0

 $^{^{}a)}$ BD: Burial Depth; $^{b)}$ $\Delta x, \Delta y: \ \,$ Lateral dimensions; $^{c)}$ $\Delta z: \ \,$ Thickness

d) G_{zz max}: Maximum vertical gravity gradient signal computed at satellite altitude (255km).

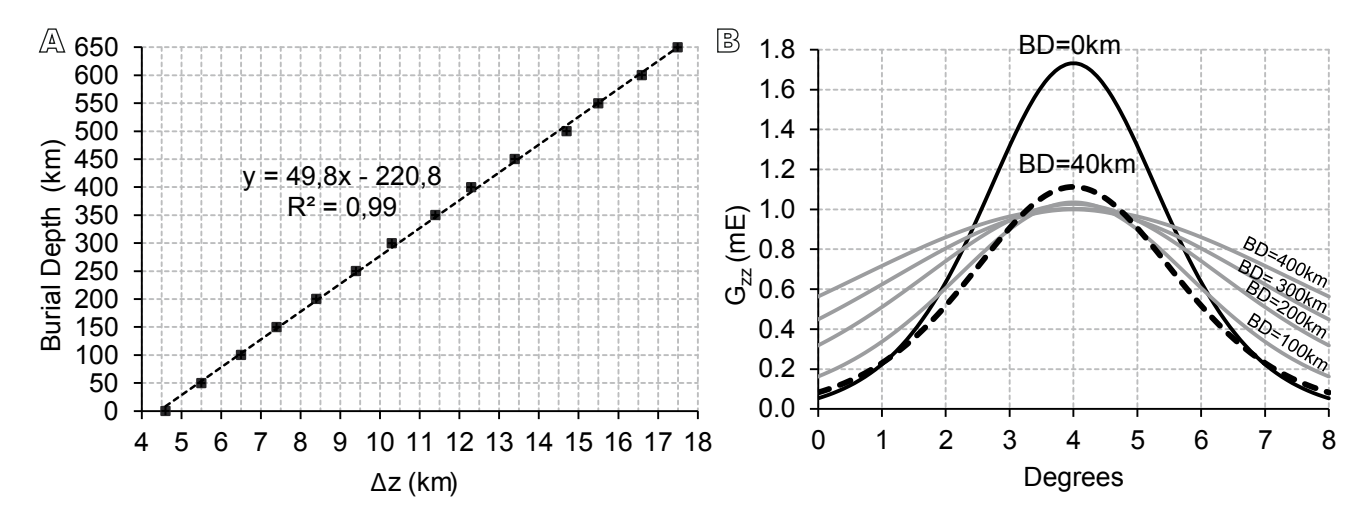


FIGURE 3. A) Thickness (Δz) of the anomalous density body as a function of its burial depth. All models have approximately the same maximum signal in the vertical component G_{zz} and keep the same aspect ratio (9:3:1). B) Gravity gradients G_{zz} (vertical axis) generated by anomalous density bodies. The horizontal axis represents the East direction. Continuous and dashed black lines correspond to a density anomaly of dimensions Δx =49.5km, Δy =16.5km, Δz =5.5km, and a density contrast of 50kg/m³ at Burial Depths (BD) of 0 and 40km, respectively. Grey lines correspond to models of different dimensions with a density contrast of 50kg/m³ at burial depths in the range of 100–400km (see Table 1).

G_{xx} component shows a quadrupole distribution with the minimum values within the anomalous body and the maximum values close to the N-S bounds of the anomaly. The G_{vv} component shows an elongated minimum centered on the anomalous body with values increasing outwards. The different shape of the G_{xx} and G_{yy} components is related to the elongated shape of the density anomaly at the low computation height. Components G_{xz} and G_{yz} display a bipolar distribution with relative extrema values distributed symmetrically with respect to the width and length axes crossing the center of the body, respectively (y and x axes). Maximum and minimum values roughly coincide with the lateral sides of the anomalous body. Finally, component G_{xy} exhibits a quadrupole pattern with alternating maximum and minimum values roughly coinciding with the corners of the anomalous body. In summary, in the case that the dimensions of the anomalous body are large relative to the computation height, the relative extrema distribution, *i.e.* the wavelength of the gravity gradient components is sensitive to the boundaries of the density anomaly, which allows for identifying its shape. It is worth noting that, due to the low computation height (5km), the half wavelength in all components is <20km, which is below the spatial resolution of GOCE.

Figure 5 shows the calculated gravity gradient components for the same anomalous density body (22.5x7.5x2.5km, $\Delta \rho = 500 \text{kg/m}^3$, $z_1 = 0 \text{km}$) computed at 255km height, the mean satellite altitude. As the computation height moves upwards, the calculated gravity gradient components show larger wavelength variations and the relative extrema of the horizontal components separate and eventually vanish. Although

the amplitude of the vertical component can be detected by GOCE, all the other components are slightly below its accuracy. Furthermore, the wavelengths of the gravity gradient variations are very far from the limits of the anomalous body and are clearly unable to delimit its shape and orientation. Note that, in this case, the main components $(G_{zz}, G_{xx} \text{ and } G_{yy})$ are insensitive to the aspect ratio of the density anomaly. On the other hand, the extrema associated with the crossed components G_{xz} and G_{vz} show an apparent rotation of 90° losing any relation with the shape of the anomaly. A similar situation occurs with the G_{xv} component where the resulting quadrupole distribution is almost symmetric and unrelated to the aspect ratio of the anomaly. Calculations at a height of 255km, varying the size of the density anomaly, and considering $\Delta \rho = 500 \text{kg/m}^3$ show that the minimum size to generate both amplitudes and variation wavelengths sensitive to the shape of the density anomaly and higher than the resolution of GOCE mission at a burial depth of 0km, are 270x90x30km (Fig. 6). On the other hand, the required minimum size increases to 585x195x65km for a prism buried at 200km depth if the density contrast is $\Delta \rho = 50 \text{kg/m}^3$. In these cases, the distance between relative extrema still reflects the aspect ratio of the anomalous body.

3D CONTINENTAL MARGIN STRUCTURES: A PROXY FOR NW-IBERIA

In the previous sections we have calculated the gravity gradient field produced by simple and isolated density anomalies. Nevertheless, in the Earth the anomalous bodies

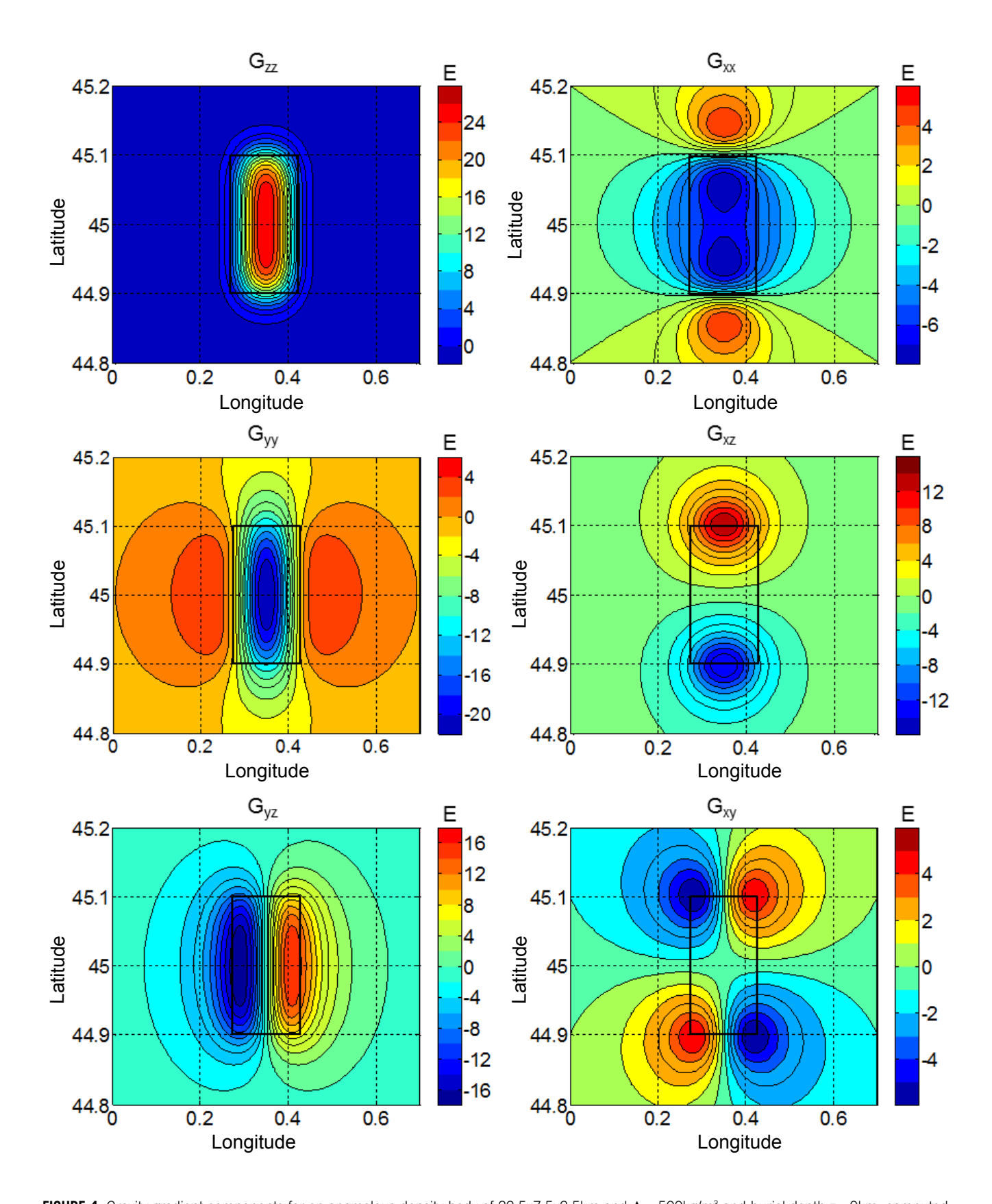


FIGURE 4. Gravity gradient components for an anomalous density body of 22.5x7.5x2.5km and $\Delta \rho$ =500kg/m³ and burial depth z_1 =0km, computed at a height of 5km.

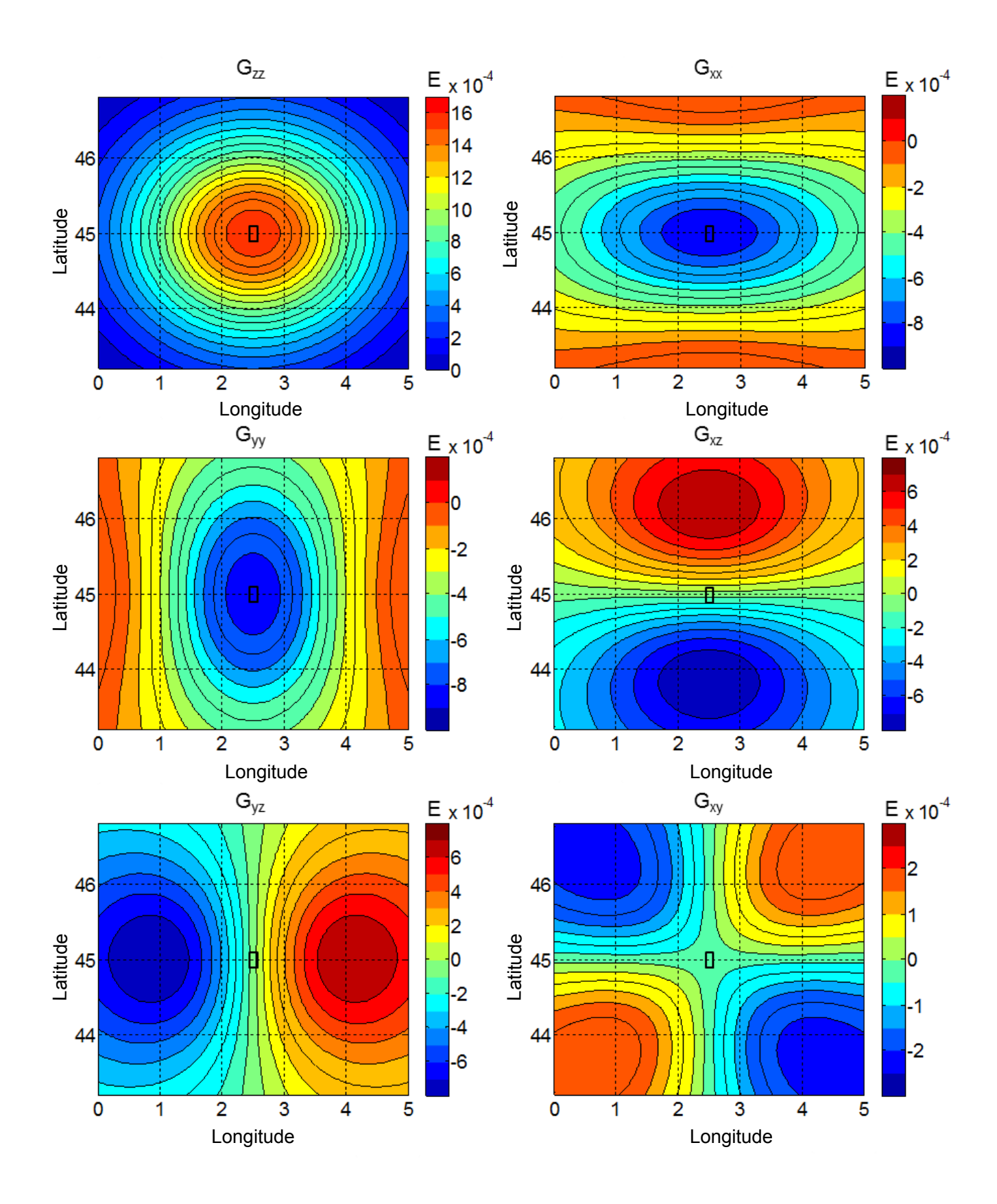


FIGURE 5. Gravity gradient components for an anomalous density body of 22.5x7.5x2.5km and $\Delta \rho$ =500kg/m³ and burial depth z_1 =0km, computed at a height of 255km, the mean satellite altitude.

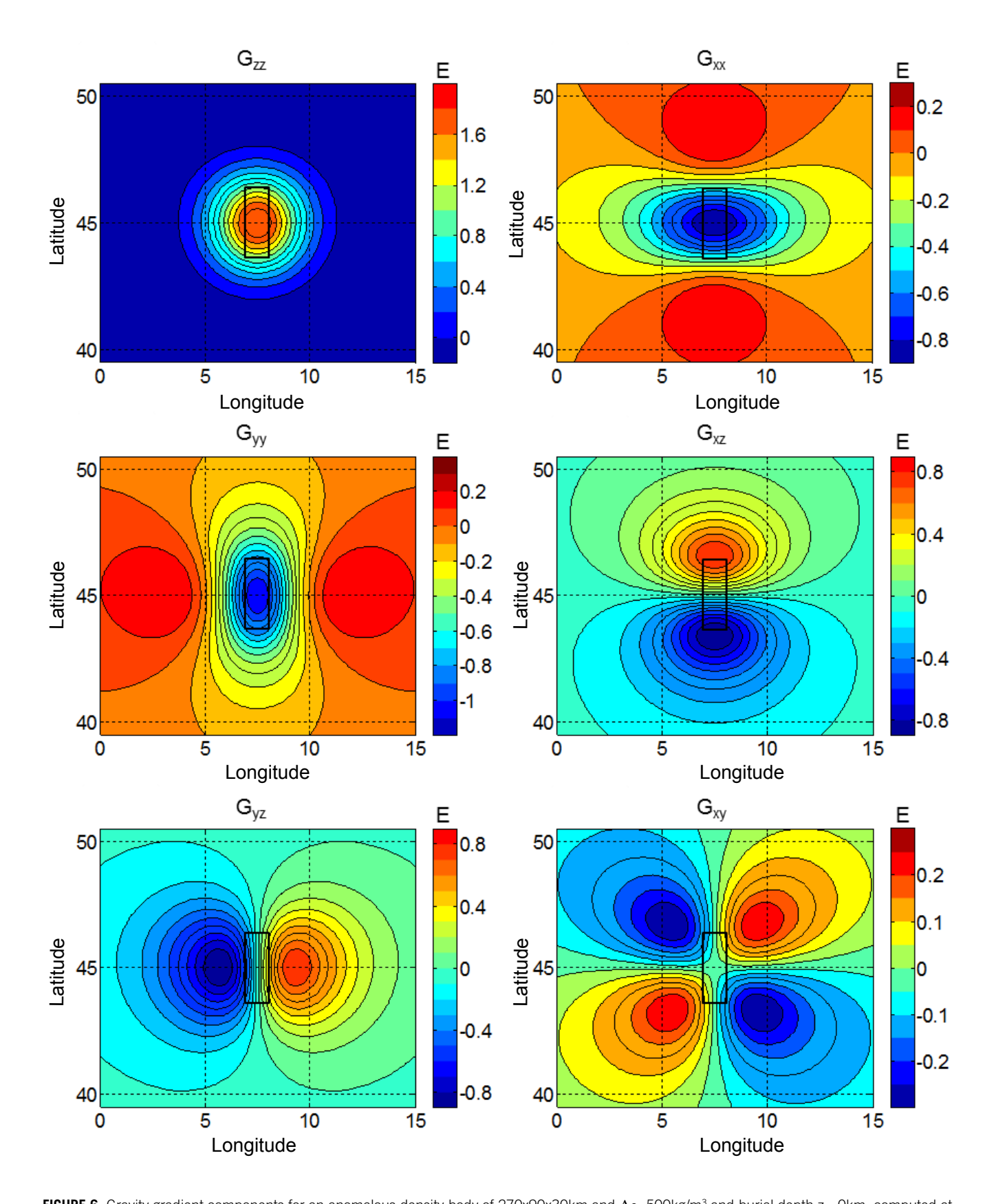


FIGURE 6. Gravity gradient components for an anomalous density body of 270x90x30km and Δp =500kg/m³ and burial depth z_1 =0km, computed at a height of 255km, the mean satellite altitude.

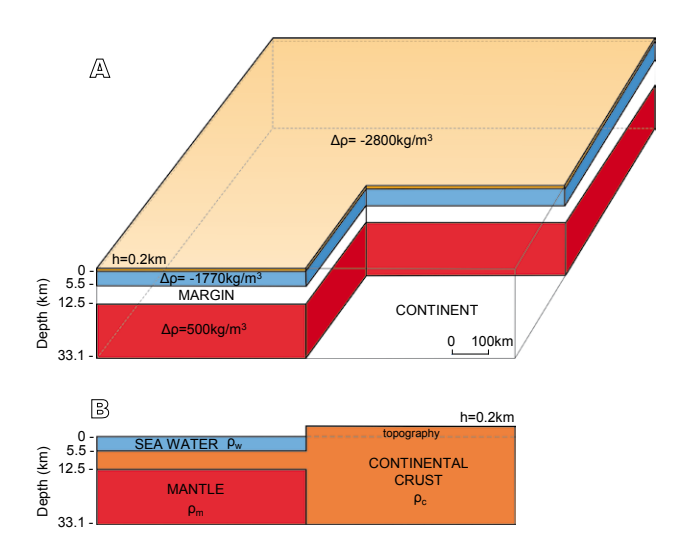


FIGURE 7. A) Cartoon showing the 3D modelled crustal structure associated with a passive continental margin resembling the NW corner of the Iberian Peninsula. Three layers have been modelled (topography: orange, seawater: blue, and lithospheric mantle: red) with a density contrast ($\Delta \rho$) relative to the crust, also seen in Fig. 7B. B) Simplified 2D crustal structure of the passive margin model and actual densities (ρ_c =2800kg/m³; ρ_m =3300kg/m³; ρ_w =1030kg/m³). The scale of the topography has been exaggerated.

are not isolated but are the result of tectonic processes that deform the crust and the lithospheric mantle in addition to surface mass transport related to erosion/sedimentation. To illustrate the application of gravity gradients to modelling large-scale crustal structures, in this section we present a first order analysis of a 3D structure that resembles the NW corner of the Iberian Peninsula and its northern and western margins (Fig. 7). It must be noted that we do not intend to reproduce the accurate crustal structure of the region, but to compare the major trends of the gravity gradient components produced by a simple 3D crustal structure with GOCO03S data.

The vertical component G_{zz} delineates the main regional trends of the margin with relative lows (<-0.2E) located at the base of the slope, while maximum values (~0.4E) are observed onshore (Fig. 8). The horizontal components, G_{xx} and G_{yy} , highlight the northern and the western margins, respectively, with a coupled positive (offshore) and negative (onshore) anomaly in a range of 0.25 to -0.25E. As expected, the weakest signal corresponds to the G_{xy} component (from 0 to -0.19E) with maximum values centered on the corner formed by both margins. Finally, the G_{xz} and G_{yz} components, with amplitudes in the range of -0.02E and 0.42E, are symmetrically opposite and show the highest amplitudes just at the shoreline of the northern and western margins, respectively.

To compare our model with the measured signal, gravity gradients are computed in the Local North

Oriented Frame (LNOF) from the disturbing potential over the Iberian Peninsula and nearby regions, including the western Mediterranean and North Africa regions (Fig. 9). All computations are incorporated on a 10x10min grid at the mean satellite altitude of 255km, taking the WGS84 as the reference ellipsoid.

The highest amplitudes in the gravity gradient components reflect the largest gravity spatial variations. The vertical component (G_{zz}) shows the strongest signal from -0.56 to 0.96E, whereas the planar components show variations from -0.58 to 0.47E for G_{xx} in S-N direction, and from -0.39 to 0.41E for G_{yy} in E-W direction. The vertical component shows the highest positive gradients over the Atlas, whilst the largest area with lowest negative values is related to the Sahara Platform. As the gravity potential satisfies the Laplace's equation, there is a direct correlation between the lateral and vertical components (G_{xx}+G_{yy}+G_{zz}=0). Comparing the G_{xx} and G_{zz} signals, we observe nearly the same but opposite anomaly patterns, since regions with higher positive amplitudes in Gzz also show higher negative amplitudes in G_{xx} and vice versa. Something similar is observed when correlating the G_{vv} and G_{zz} signals, though in this case the anomaly pattern of the lateral component is slightly different, highlighting the structures oriented N-S like the western Iberian margin and the Calabrian Arc. Crossed components are sensitive to the borders of the major structures and its orientation.

The gravity gradient field derived from the synthetic model (Fig. 8) shows a very similar pattern in the large wavelengths than that obtained from the GOCO03S in the NW Iberian Peninsula and its associated northern and western margins (Fig. 9). Nevertheless, some differences are observed in the signal amplitudes that are as much as 0.3E in the G_{zz} component and 0.1 and 0.05E in the G_{xx} and G_{yy} components, respectively, the crossed components showing similar amplitudes. A different case is the South-Iberia and North-Africa regions (Fig. 9), where the measured gravity gradient pattern is not easily identifiable with a simple margin structure, which could be explained by the presence of sublithospheric anomalous bodies (e.g. Spakman and Wortel, 2004; Fullea et al., 2010, 2014; Díaz and Gallart, 2014; Villaseñor et al., 2015).

DISCUSSION

Gravity gradients are proven to be very sensitive to the shape of a given anomalous body or geological structure provided that there is sufficient density contrast with the surrounding medium. The six gradient components help in constraining the size and position of the lateral

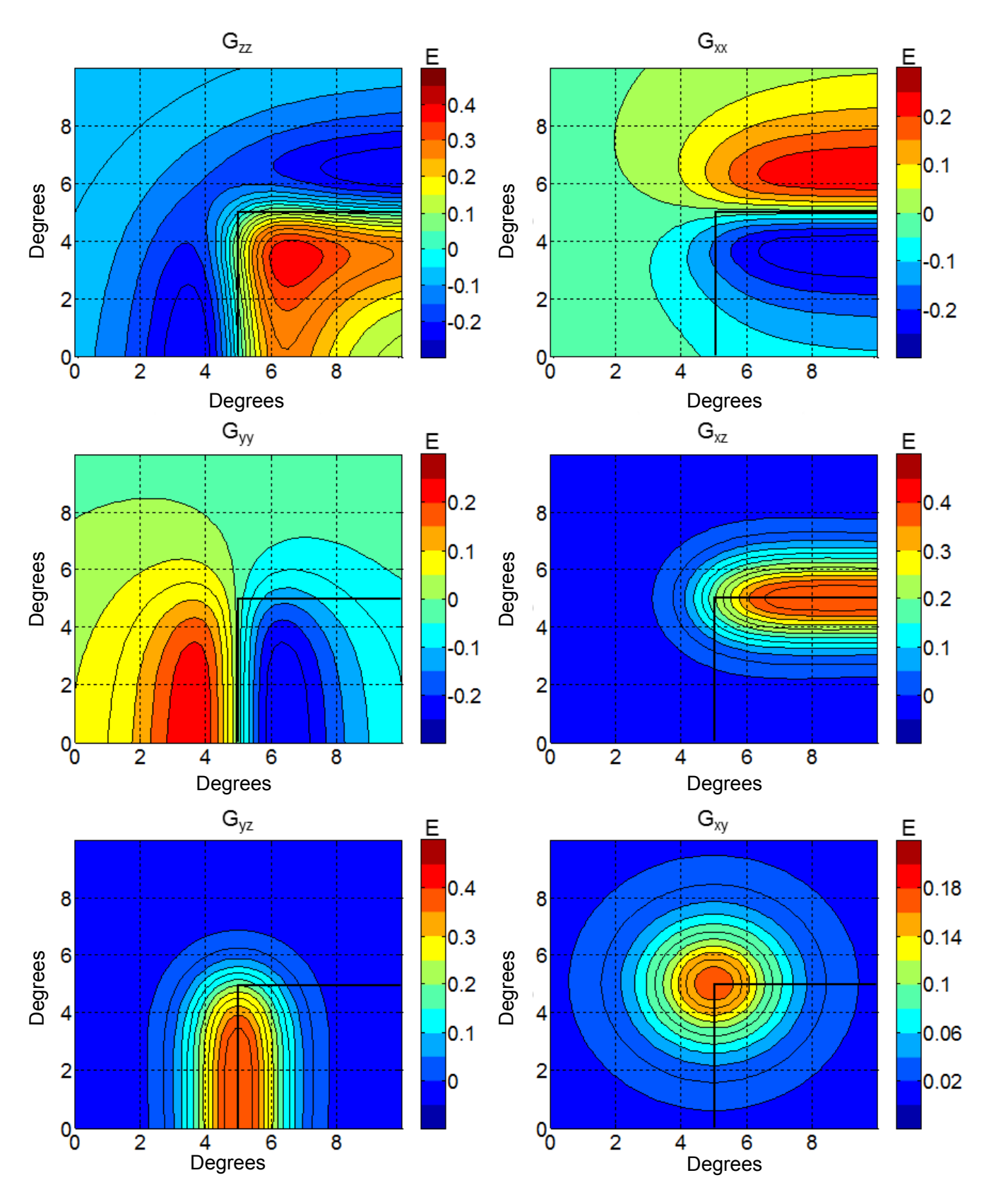


FIGURE 8. Gravity gradient components (Eötvös) generated from a synthetic model of a 3D passive continental margin using spherical approximation. Black lines delineate the location of the margin. The Y axis orientation has been changed to be comparable with the LNOF, where the Y axis is pointing to the West.

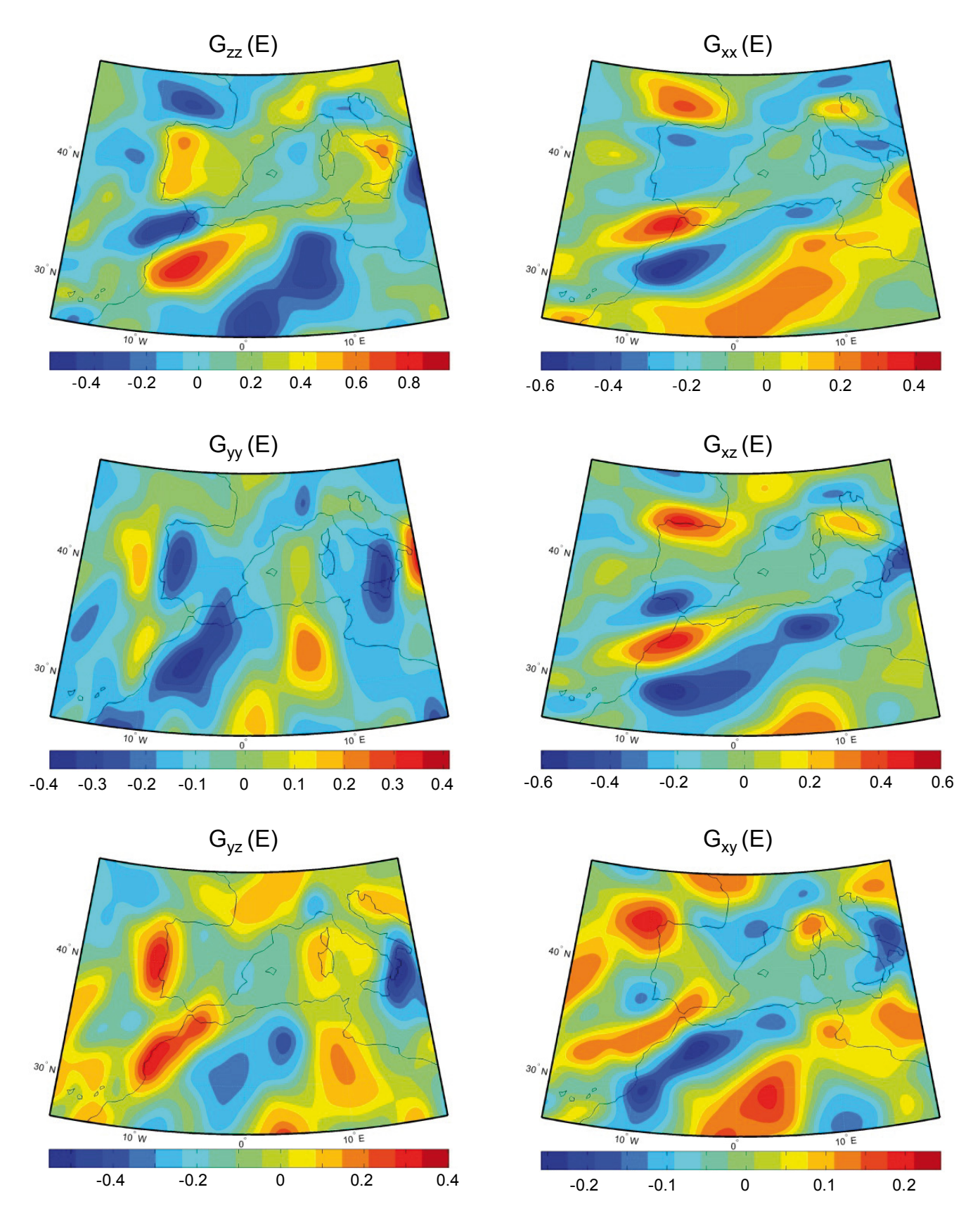


FIGURE 9. Gravity gradient components (Eötvös) derived from GOCO03S computed at 255km mean satellite altitude over the Iberian Peninsula and nearby regions. Gradients are computed in the LNOF, where the X axis is aligned with the North direction, the Y axis in the West direction and Z axis is pointing up.

sides of the structure as well as its burial depth. This is particularly true when measurements are relatively close to the anomaly as the signal vanishes rapidly due to its dependence with (L/r^3) . The mean satellite altitude of the GOCE mission is 255km and then, the calculated gradients at this height show a noticeable reduction in its amplitude and a large increase in its wavelength.

According to our resolution tests, a rectangular prism anomaly with a density contrast of 500kg/m^3 and a burial depth between 0–40km, requires a minimum size of 22.5 x 7.5 x 2.5 km to generate a detectable signal of 1mE amplitude in the G_{zz} component. However, this size must be multiplied by a factor f=12 when using the wavelengths of all gravity gradient components to determine the precise position and shape of the anomalous structure.

When the density contrast is reduced to 50kg/m^3 , the required size of the structure to be detected in the G_{zz} component must be multiplied by a factor f=1.8, for a burial depth z_1 =0km; f=3.4, for z_1 =200km; or f=4.9, for z_1 =400km. Moreover, the required minimum size increases to $585 \times 195 \times 65 \times 65 \times 195 \times$

These calculations evidence that gravity gradients computed at satellite altitude can be used to determine mid-to-large scale structures, depending on their burial depths. Structures of hundreds km long are typical for tectonic processes related to orogenesis or rifting, in which the crust and the lithospheric mantle undergo thickening or thinning. Larger structures can also be related to sinking lithospheric slabs associated with subduction, and to convection or chemical anomalies in the sublithospheric mantle, as revealed by seismic tomography. In this regard, the main advantage of using all gravity gradient components is their sensitivity to sharp changes in the gravity field and therefore, to the lateral boundaries of the anomalous structures. It is also expected that GOCE mission can contribute to analyze and refine the Gravitational Centroid Moment Tensor solutions associated with the mass redistribution produced by large earthquakes (e.g. Sumatra-2004, Tohoku-2011) previously calculated from GRACE satellite mission data (e.g. Cambiotti and Sabadini, 2012, 2013).

It should be noted, however, that the presented resolution tests are based on an isolated density anomaly corresponding to a prism with a fixed aspect ratio. This is not the general case in nature, where density anomalies are placed at different depths resulting in a complex superposition of individual signatures. Using different

aspect ratios will modify the calculated signal, although when the anomalous mass is equivalent and the lateral dimensions are realistic, these changes are not significant. In addition, the gravity gradient will be sensitive to the inclination of the lateral sides of the anomalous body, such that a regular prism, as that considered in the resolution test, tends to maximize the signal. Finally, the high satellite altitude together with the burial depth of the density anomalies contributes to the filtered and somewhat blurred final image of the computed gravity gradient components.

Bearing in mind all these aspects, we have applied a very simple model to the northwestern corner of the Iberian Peninsula, which is characterized by a 3D structure formed by the northern and western Iberian-Atlantic passive continental margins. As we have not removed the signal of topographic masses from GOCE data, we have computed the average topography and water layer effect so that measured and calculated values can be directly compared.

The signal observed in all the gravity gradient components is dominated by the crustal thinning associated with the passive continental margins and the corresponding isostatic response. Differences between measured and calculated gravity gradient components are attributed to both short wavelength departures of the averaged topography of our 3D model and second order structures within the crust and/or the lithospheric mantle not considered in our approach.

CONCLUSIONS

The main goal of this study was to analyze the resolution, in terms of shape, minimum size, and density contrast of anomalous bodies related to geological structures that can be identified from GOCE gravity gradient data. From the presented models, we can draw the following conclusions:

i) Gravity gradients obtained in the GOCE mission can detect a buried density anomaly as long as the amplitude of the signal in the vertical component is $G_{zz} \ge 1$ mE and the half wavelength is >80km. When the dimensions of the anomalous body are large relative to the computation height, the position of the relative extrema (maximum and minimum values) of the gravity gradient components allow for identifying its shape, orientation and burial depth.

ii) For given computation heights and density contrasts, there is a linear relationship between the burial depth and the thickness of the anomalous density body producing the same amplitude in the G_{zz} component, when using the fixed aspect ratio of 9:3:1.

- iii) For crustal density anomalies, the minimum dimensions of an anomalous body that can be resolved by the G_{zz} component computed at a height of 255km, with a density contrast of $\Delta \rho$ =500kg/m³, and a burial depth of 0–40km, is Δx =22.5km, Δy =7.5km, and Δz =2.5km.
- iv) For crustal and upper mantle density anomalies with $\Delta \rho = 50 kg/m^3$ and a burial depth from 0 to 650km, the minimum dimensions for a body to be detected must be multiplied by a factor, relative to a crustal density anomaly with $\Delta \rho = 500 kg/m^3$, of 1.8, 3.4, 4.9 or 7 for burial depths of 0, 200, 400 and 650km, respectively.
- v) Determining the size and orientation of a crustal density anomaly from the position of the relative extreme (wavelength of the signal) of the gravity gradient components, requires a minimum size of $270 \times 90 \times 30 \text{km}$, *i.e.* a factor 12 for a $\Delta \rho = 500 \text{kg/m}^3$ and a computation height of 255 km. This factor rises up to $26 \times (585 \times 195 \times 65 \text{km})$ for a body with $\Delta \rho = 50 \text{kg/m}^3$ and buried at a depth of 200 km.
- vi) The application to the 3D case of NW-Iberia shows that the signal of all gravity gradient components is dominated by the crustal thinning associated with the passive continental margins and the corresponding isostatic response. Misfits are related to short wavelength departures of the averaged topography considered in our model and to second order crustal and/or lithospheric mantle structures.

ACKNOWLEDGMENTS

This work is part of the projects ALPIMED (PIE-CSIC-201530E082) and MITE (CGL2014-59516-P).

REFERENCES

- Afonso, J.C., Fullea, J., Griffin, W.L., Yang, Y., Jones, A.G., Yang, Y., Connolly, J.A.D., O'Reilly, S.Y., 2013. 3-D multiobservable probabilistic inversion for the compositional and thermal structure of the lithosphere and upper mantle. In: *A priori* petrological information and geophysical observables. Journal of Geophysical Research: Solid Earth, 118, 2586-2617.
- Barton, P.J., 1986. The relationship between seismic velocity and density in the continental crust a useful constraint? Geophysical Journal Royal Astronomical Society, 87, 195-208.
- Barzaghi, R., Reguzzoni, M., Borghi, A., de Gaetani, C., Sampietro, D., Marotta, A.M., 2015. Global to local moho estimate based on GOCE geopotential model and local gravity data. International Association of Geodesy Symposia, 275-282.
- Bingham, R.J., Knudsen, P., Andersen, O., Pail, R., 2011. An initial estimate of the North Atlantic steady-state geostrophic circulation from GOCE. Geophysical Research Letters, 38(1), L01606, DOI: 10.1029/2010GL045633

- Bouman, J., Fuchs, M.J., 2012. GOCE gravity gradients *versus* global gravity field models. Geophysical Journal International, 189, 846-850.
- Bouman, J., Ebbing, J., Fuchs, M., 2013. Reference frame transformation of satellite gravity gradients and topographic mass reduction. Journal of Geophysical Research: Solid Earth, 118, 759-774.
- Bouman, J., Ebbing, J., Meekes, S., Fattah, R.A., Fuchs, M., Gradmann, S., Haagmans, R., Lieb, V., Schmidt, M., Dettmering, D., Bosch, W., 2015. GOCE gravity gradient data for lithospheric modeling. International Journal of Applied Earth Observation and Geoinformation, 35, 16-30.
- Bouman, J., Ebbing, J., Fuchs, M., Sebera, J., Lieb, V., Szwillus, W., Haagmans, R., Novak, P., 2016. Satellite gravity gradient grids for geophysics. Scientific Reports, 6:21050, 11pp. DOI: 10.1038/srep21050
- Braitenberg, C., Mariani, P., De Min, A., 2013. The European Alps and nearby orogenic belts sensed by GOCE. Bollettino di Geofisica, Teorica ed Applicata, 54, 321-334.
- Brocher, T.M., 2005. Empirical Relations between Elastic Wavespeeds and Density in the Earth's Crust. Bulletin of the Seismological Society of America, 95, 2081-2092. DOI:10.1785/0120050077
- Cambiotti, G., Sabadini, R., 2012. A source model for the great 2011 Tohoku earthquake (Mw=9.1) from inversion of GRACE gravity data. Earth and Planetary Science Letters, 335-336, 72-79. DOI: 10.1016/j.epsl.2012.05.002
- Cambiotti, G., Sabadini, R., 2013. Gravitational seismology retrieving Centroid-Moment-Tensor solution of the 2011 Tohoku earthquake. Journal of Geophysical Research: Solid Earth, 118, 183-194. DOI: 10.1029/2012JB009555
- Cammarano, F., Tackley, P., Boschi, L., 2011. Seismic, petrological and geodynamical constraints on thermal and compositional structure of the upper mantle: Global thermochemical models. Geophysical Journal International, 187, 1301-1318.
- Christensen, N.I., Mooney, W.D., 1995. Seismic velocity structure and composition of the continental crust: a global view. Journal of Geophysical Research, 100, 9761-9788.
- Díaz, J., Gallart, J., 2014. Seismic anisotropy from the Variscan core of Iberia to the Western African Craton: New constrains on upper mantle flow at regional scales. Earth and Planetary Science Letters, 394, 48-57.
- Fadel, I., van der Meijde, M., Kerle, N., Lauritsen, N., 2015. 3D object-oriented image analysis in 3D geophysical modelling: Analysing the central part of the East African Rift System. International Journal of Applied Earth Observation and Geoinformation, 35, 44-53.
- Fecher, T., Pail, R., Gruber, T., 2015. Global gravity field modeling based on GOCE and complementary gravity data. International Journal of Applied Earth Observation and Geoinformation, 35, 120-127.
- Floberghagen, R., Fehringer, M., Lamarre, D., Muzi, D., Frommknecht, B., Steiger, C., Piñeiro, J., da Costa, A., 2011. Mission design, operation and exploitation of the gravity field and steady-state ocean circulation explorer mission. Journal of Geodesy, 85, 749-758.

- Fuchs, M.J., Bouman, J., 2011. Rotation of GOCE gravity gradients to local frames. Geophysical Journal International, 187, 743-753.
- Fullea, J., Fernàndez, M., Afonso, J.C., Vergés, J., Zeyen, H., 2010. The structure and evolution of the lithosphereasthenosphere boundary beneath the Atlantic-Mediterranean Transition Region. Lithos, 120, 74-95.
- Fullea, J., Muller, M.R., Jones, A.G., Afonso, J.C., 2014. The lithosphere-asthenosphere system beneath Ireland from integrated geophysical-petrological modeling II: 3D thermal and compositional structure. Lithos, 189, 49-64.
- Fullea, J., Rodríguez-González, J., Charco, M., Martinec, Z., Negredo, A., Villaseñor, A., 2015. Perturbing effects of sublithospheric mass anomalies in GOCE gravity gradient and other gravity data modelling: Application to the Atlantic-Mediterranean transition zone. International Journal of Applied Earth Observation and Geoinformation, 35, 54-69.
- Globig, J., Fernàndez, M., Torne, M., Vergés, J., Robert, A., Faccenna, C., 2016. New insights into the crust and lithospheric mantle structure of Africa from elevation, geoid, and thermal analysis. Journal of Geophysical Research: Solid Earth, 121, 5389-5424.
- Godah, W., Krynski, J., 2013. Evaluation of recent goce geopotential models over the area of Poland. Acta Geodynamica et Geomaterialia, 10, 379-386.
- Hirt, C., Kuhn, M., Featherstone, W.E., Gtötl, F., 2012. Topographic/isostatic evaluation of new-generation GOCE gravity field models. Journal of Geophysical Research: Solid Earth, 117, B05407, 16pp. DOI: 10.1029/2011JB008878
- Holzrichter, N., Ebbing, J., 2016. A regional background model for the Arabian Peninsula from modeling satellite gravity gradients and their invariants. Tectonophysics, 692, 86-94. DOI: 10.1016/j.tecto.2016.06.002
- Köther, N., Götze, H.-J., Gutknecht, B.D., Jahr, T., Jentzsch, G.,
 Lücke, O.H., Mahatsente, R., Sharma, R., Zeumann, S., 2012.
 The seismically active Andean and Central American margins:
 Can satellite gravity map lithospheric structures? Journal of
 Geodynamics, 59-60, 207-218. DOI: 10.1016/j.jog.2011.11.004
- Mariani, P., Braitenberg, C., Ussami, N., 2013. Explaining the thick crust in Paraná basin, Brazil, with satellite GOCE gravity observations. Journal of South American Earth Sciences, 45, 209-223.
- Martinec, Z., Fullea, J., 2015. A refined model of sedimentary rock cover in the southeastern part of the Congo basin from GOCE gravity and vertical gravity gradient observations. International Journal of Applied Earth Observation and Geoinformation, 35, 70-87.
- Mayer-Gürr, T., Pail, R., Gruber, T., Fecher, T., Rexer, M., Schuh, W.D., Kusche, J., Brockmann, J.M., Krasbutter, I., Becker, S., Eicker, A., Schall, J., Rieser, D., Zehentner, N., Baur, O., Höck, E., Hausleitner, W., Maier, A., Krauss, S., Jäggi, A., Meyer, U., Prange, L., 2012. The new combined satellite only model GOCO03s. International Symposium on Gravity, Geoid and Height Systems, Venice, Italy (Poster). [Available at: http://www.goco.eu]

- Maystrenko, Y., Scheck-Wenderoth, M., 2009. Density contrasts in the upper mantle and lower crust across the continent-ocean transition: Constraints from 3-D gravity modelling at the Norwegian margin. Geophysical Journal International, 179, 536-548.
- Mysen, E., 2015. A mascon adjustment of the Earth's gravity field using GOCE gradiometer data. Journal of Applied Geodesy, 9, 63-71.
- Pal, S.K., Majumdar, T.J., 2015. Geological appraisal over the Singhbhum-Orissa Craton, India using GOCE, EIGEN6-C2 and in situ gravity data. International Journal of Applied Earth Observation and Geoinformation, 35, 96-119.
- Reguzzoni, M., Sampietro, D., 2015. GEMMA: An Earth crustal model based on GOCE satellite data. International Journal of Applied Earth Observation and Geoinformation, 35, 31-43.
- Saad, A.H., 2006. Understanding gravity gradients A tutorial. Leading Edge (Tulsa, OK), 25, 942-949.
- Spakman, W., Wortel, M.J.R., 2004. A tomographic view on the Western Mediterranean geodynamics. In: Cavazza, W., Roure, F., Spakman, W., Stampfli, G., Ziegler, P., (eds.). The TRANSMED Atlas-the Mediterranean Region from Crust to Mantle. Springer, Berlin, Heidelberg, 31-52.
- Torne, M., Fernàndez, M., Vergés, J., Ayala, C., Salas, M.C., Jimenez-Munt, I., Buffett, G.G., Díaz, J., 2015. Crust and mantle lithospheric structure of the Iberian Peninsula deduced from potential field modeling and thermal analysis. Tectonophysics, 663, 419-433. DOI: 10.1016/j. tecto.2015.06.003
- Uieda, L., Barbosa, V.C.F., Braitenberg, C., 2015. Tesseroids: Forward-modeling gravitational fields in spherical coordinates. Geophysics, 81(5), F41-F48. DOI: 10.1190/ GEO2015-0204.1
- van der Meijde, M., Pail, R., Bingham, R., Floberghagen, R., 2015a. GOCE data, models, and applications: A review. International Journal of Applied Earth Observation and Geoinformation, 35, 4-15.
- van der Meijde, M., Pail, R., Bingham, R., 2015b. Introduction to the special issue on GOCE Earth science applications and models. International Journal of Applied Earth Observation and Geoinformation, 35, 1-3.
- Villaseñor, A., Chevrot, S., Harnafi, M., Gallart, J., Pazos, A., Serrano, I., Córdoba, D., Pulgar, J.A., Ibarra, P., 2015. Subduction and volcanism in the Iberia-North Africa collision zone from tomographic images of the upper mantle. Tectonophysics, 663, 238-249.

Manuscript received July 2017; revision accepted November 2017; published Online February 2018.